



Catalytic palladium nanoparticles supported on nanoscale MOFs: a highly active catalyst for Suzuki–Miyaura cross-coupling reaction



Linjie Zhang^{a,b}, Zixue Su^a, Feilong Jiang^a, Youfu Zhou^{a,*}, Wentao Xu^a,
Maochun Hong^{a,*}

^a Key Laboratory of Optoelectronic Materials Chemistry and Physics, Fujian Institute of Research on the Structure of Matter, Chinese Academy of Sciences, Fuzhou 350002, China

^b University of Chinese Academy of Sciences, Beijing 100049, China

ARTICLE INFO

Article history:

Received 22 May 2013

Received in revised form 3 August 2013

Accepted 20 August 2013

Available online 27 August 2013

Keywords:

Palladium

Nanoscale metal-organic frameworks

Catalysis

Suzuki–Miyaura cross-coupling

ABSTRACT

Pd nanoparticles have been successfully supported on nanoscale metal-organic frameworks (NMOFs) by using a simple and effective microwave-assisted impregnation process. The resulting composite, representing as a highly active NMOFs supported metal nanoparticles catalyst for the Suzuki cross-coupling reaction between aryl/heteroaryl halides and arylboronic acids, is well characterized, and its high activity and good recyclability are discussed in details. It reveals that, compared to the corresponding bulk MOFs and conventional active carbon materials, nanoscale MOFs as novel support materials for heterogeneous catalysts can exhibit superior performance in the catalytic reactions.

© 2013 Elsevier Ltd. All rights reserved.

1. Introduction

Metallic nanoparticles (NPs) with controllable morphology and dimension can show dramatically different physicochemical properties from their bulk materials, due to the quantum effects resulting from scale miniaturization.¹ They are promising in a variety of applications ranging from catalysis² to optoelectronic devices³ and even to advanced biomedical utilities.⁴ Therefore, much effort has been devoted to explore effective and facile synthetic strategies to get well-defined metal NPs.⁵ Especially, when metallic NPs are used as heterogeneous catalyst in some reactions such as the Pd catalyzed Suzuki cross-coupling reaction, the requirement of a special type of surface atoms or a synergism of surface atoms is significantly influenced by the alteration of the particle size and shape.⁶

Previously established approaches have enabled controllable synthesis of NPs with a variety of shapes and dimensions.⁷ However, there still remains challenging for the synthesis of sub-5 nm particles. In the recent years, porous materials have been employed as hard templates for the synthesis of nanoparticles, which becomes a prevailing protocol to prepare metallic NPs in sizes of several nanometers relying on the confinement effect in their

tunable micro/meso-channels.⁸ The micro/mesoporous materials can also act as dispersive mediums for metal NPs, which is of importance since the nanoscale dimensions of NPs render them chemically very reactive and/or physically aggregative, and the homogeneous distributions of the active sites are very crucial for the catalytic performance. These host micro/mesoporous materials of different natures, such as zeolites,⁹ carbon polymorphs,¹⁰ mesoporous silica,⁸ polymers,¹¹ porous metal oxides,¹² and other molecular sieves have been intensively investigated for many years in the field of catalytic metallic supports.

Recently, metal-organic frameworks (MOFs), resulting from the organometallic complexes held together by metal ions, have emerged as a new family of solid matrices to support and disperse metal NPs for catalysis applications owing to their high surface area, porosity, chemical tunability, and well-defined pore structure.^{13–15} Although the template-directed synthesis of the metal NPs in the channels of MOFs (denoted as M@MOFs) is practicable,^{16–18} most reported M@MOFs show that the dimensions of the metal NPs obtained are usually several times larger than those of the MOFs pores,^{19–21} typically 3–5 nm versus 1–2 nm, partially owing to the decomposition of the frameworks around the aggregated metal clusters. Usually, the metal NPs tend to locate at the external surface of the MOFs straightforwardly, expressed as M/MOFs, other than in the pores/channels, although good catalytic performances can still be observed.^{22–24} Today, it is still very challenging for the controllable growth of metal NPs in the pores or

* Corresponding authors. Tel.: +86 591 8379 2620; fax: +86 591 8379 4946; e-mail addresses: yfzhou@fjirsm.ac.cn (Y. Zhou), hmc@fjirsm.ac.cn (M. Hong).

channels of the MOFs. MOFs, as a novel class of porous supports, have advantages over other inorganic porous materials in some aspects, especially for the convenient adjustment of the composition and structure. However, little attention has been paid to the nanoscale MOFs (NMOFs) incorporated with catalytic metal NPs till now. As a new class of highly tailorable nanoscale materials, NMOFs have experienced rapidly increasing attention in the past five years yet still in their infancy.²⁵ They can not only maintain the rich structural diversity and physicochemical properties of bulk MOFs but also achieve novel or enhanced properties in applications as diverse as gas storage,²⁶ separation,^{27,28} biomedical imaging²⁹ and drug delivery,^{30,31} owing to the particle dimensions ranging from tens to hundreds of nanometers. So far, a variety of synthetic routes that have been developed for inorganic and organic polymeric nanoparticles can be used to produce NMOFs, and various morphologies, such as sphere particles, polyhedrons, tubes, rods and hierarchical nanostructures have already been synthesized.²⁵ However, there is still a lack of knowledge concerning the key parameters for the precise control over the dimensions of NMOFs.

As a contribution to the domain of nanoscale metal-organic frameworks and their utilizations as templates and novel supports for metal loading, the present work will report and discuss on the synthesis, structural characterization and the catalytic activity toward Suzuki–Miyaura cross-coupling reactions of a composite material formed by generation of Pd NPs in nanoscale scandium-organic frameworks. The NMOFs, self-assembling from scandium(III) and multiple-carboxyl bridging ligand of trimesic acid (denoted as ScBTC), were synthesized by a facile surfactant-assisted microwave irradiation method, and the further support of catalytic palladium NPs was accomplished by a simple and effective microwave-assisted impregnation process.

2. Results and discussion

2.1. Characterizations of ScBTC NMOFs and Pd-NMOFs

The MOFs structures of ScBTC materials have been verified by repeated experiments under various synthetic conditions and careful characterizations, though the corresponding single crystals are hardly obtained yet. The powder X-ray diagrams (PXRD) of the as-synthesized ScBTC NMOFs with and without Pd loading confirm that the crystallinity of the NMOFs was unaffected after the impregnation process (Fig. 1a and b), despite a slight modification of the diffraction peak intensities. The sharp peaks indicate good

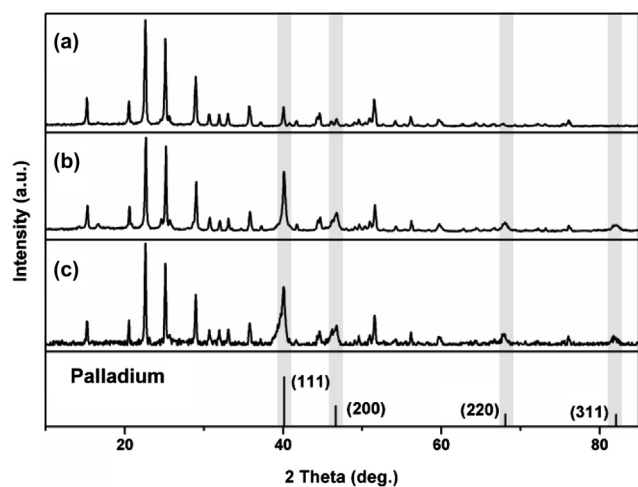


Fig. 1. Powder X-ray diffraction patterns of ScBTC NMOFs and Pd-NMOFs. (a) ScBTC NMOFs; (b) Pd-ScBTC NMOFs catalyst; (c) Pd-ScBTC NMOFs catalyst after five catalytic cycles. (Palladium from JCPDS # 05-0681).

crystallinity of the ScBTC NMOFs, while the broad peaks of Pd species could be attributed to the nanoscale dimension. Compared with the ScBTC NMOFs, the diffraction peaks of Pd supported NMOFs at $2\theta=40.1^\circ$ and 46.6° are enhanced both in intensity and width due to the overlap of diffraction peaks between ScBTC NMOFs and the (111) and (200) reflections of a Pd cubic cell ($Fm\bar{3}m$) (α -phase). The results identify the compositions of Pd NPs and the ScBTC NMOFs clearly, which will be called Pd-ScBTC NMOFs in the following.

As shown in the scanning electron microscopy (SEM) and transmission electron microscopy (TEM) images (Fig. 2a and b), the as-synthesized ScBTC NMOFs crystals mostly present as regular cuboids with smooth surface and uniform size in length of ca. 250 nm despite few irregular intergrowth of crystals. TEM images of Pd loaded ScBTC NMOFs show no significant changes in morphology as compared with the ScBTC NMOFs (Fig. 3). The Pd NPs exist as black dots with a mean size of (3.32 ± 0.54) nm calculated from 200 randomly selected particles (Fig. S1). The supporting NMOFs show gray color with lighter contrast due to their compositions of light elements (low Z value). Pd NPs were well dispersed on the ScBTC NMOFs and no significant aggregation was observed. High-resolution TEM images reveal the high crystallinity of near spherical like Pd NPs. The clear crystal lattice fringes with a spacing of 0.226 nm, correspond to the (111) facets of palladium. The energy dispersive spectroscopy (EDS) further confirms the existence of Pd elements for the catalyst in the analysis area (Fig. S2).

N_2 sorption isotherms (Fig. 4) of the ScBTC NMOFs and Pd-ScBTC NMOFs both exhibit a Type I behavior typical for microporous materials. The steep increase in the adsorbed volume at low relative pressure reveals the presence of microporosity in the samples. The specific surface areas for ScBTC NMOFs and Pd-ScBTC NMOFs are 503 and $361\text{ m}^2\text{ g}^{-1}$ by using multiple-point BET method in the relative pressure range of $p/p_0=0.06\text{--}0.25$, respectively. Using the Dubinin–Radushkevich equation, the micropore volumes of ScBTC NMOFs and Pd-ScBTC NMOFs are calculated as 0.16 and $0.09\text{ cm}^3\text{ g}^{-1}$, respectively. The total pore volumes, as calculated at relative pressure $p/p_0=0.99$, are 0.34 and $0.16\text{ cm}^3\text{ g}^{-1}$ for ScBTC NMOFs and Pd-ScBTC NMOFs, respectively. The pore size distributions calculated by using the Horvath–Kawazoe model for the adsorption branch of the isotherms prove that the micropores of NMOFs are less than 2 nm and the dominant pores are at 0.78 nm. While after the embedding of Pd NPs, the two peaks of the pore size distribution curve of ScBTC NMOFs, which originally located at 1.42 and 1.97 nm disappear, remaining a slightly shift peak around 0.75 nm (see the inset of Fig. 4). The decrease in surface areas, pore diameters, micropore and total volumes indicates the occupation and/or blocking of the cavities of ScBTC NMOFs by the highly dispersed Pd NPs.

Since the particle sizes are bigger than the pore sizes, the Pd NPs can hardly access into the pore channels of the NMOFs, they are assumed to be mainly located at the surface as in the case of metal NPs located on MOF-5, ZIF-8, and MIL-101 materials.^{19,22,24} However, it could not exclude that a certain ratio of Pd NPs with size larger than the pore size can still deposit into the pores of the NMOFs in our case. As soon as many tiny Pd clusters with several atoms are initially formed inside the pores, they rapidly agglomerate until a certain point is reached when no other feeding particles are available to form bigger nanoparticles, maintaining a size bigger than the pores along with partially decomposition of the frameworks of the supports.¹⁶ Moreover, even when some tiny Pd NPs ($<1\text{ nm}$) are embedded within the pores of NMOFs, TEM images would become distorted and ambiguous due to accumulated charges,²⁴ which make the identification of tiny Pd NPs very difficult. Indeed, due to the impregnation method used, metal loading can occur both on the surface and within the pores, and the effective diameter of the pores determines the amount of

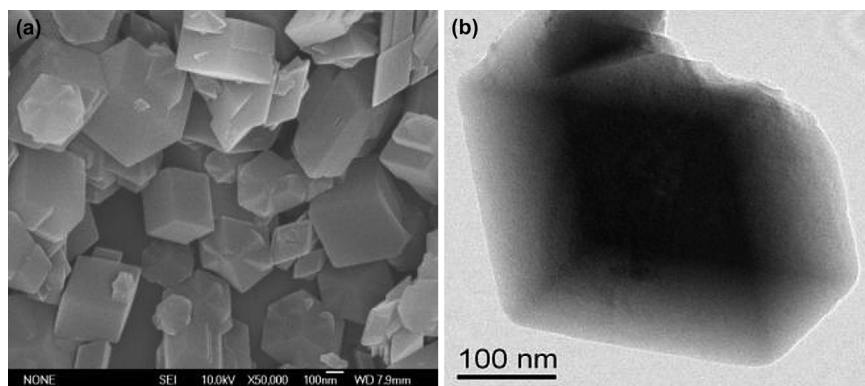


Fig. 2. Representative SEM (a) and TEM (b) images of ScBTC NMOFs.

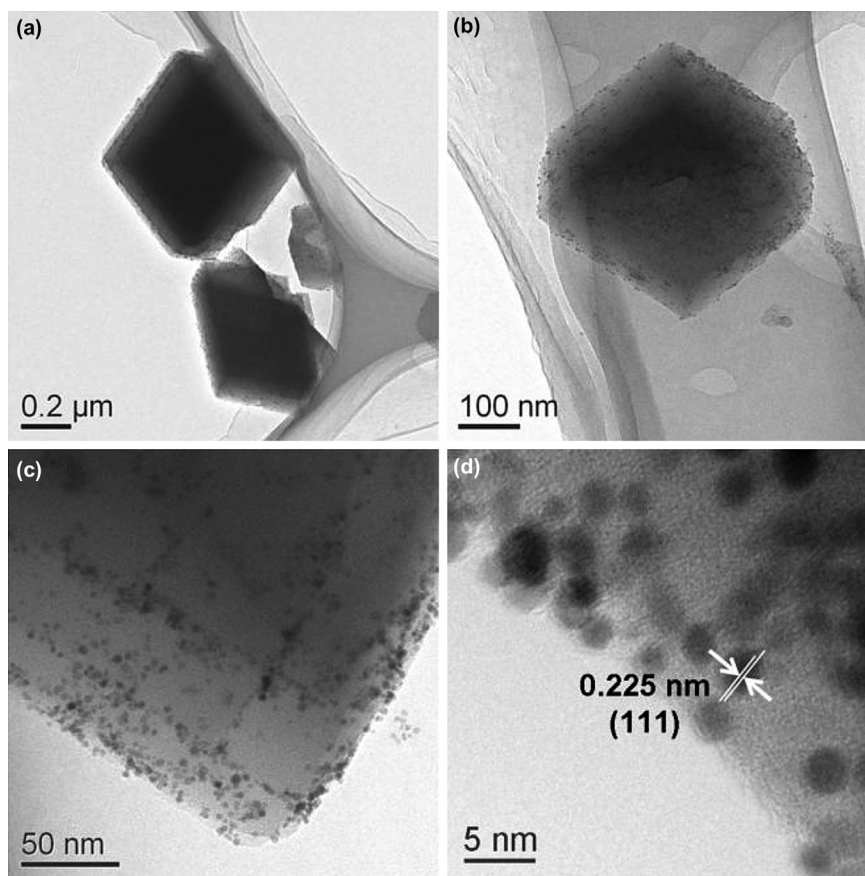


Fig. 3. TEM images of Pd-ScBTC NMOFs. (a) Overall view of Pd supported on ScBTC NMOFs; (b, c) Pd NPs dispersed on a single nanocuboid; (d) a close vision of Pd NPs by HRTEM image.

trapped PdCl_4^{2-} precursors and the subsequent metal NPs after reduction. The microporous ScBTC NMOFs preserve free pore diameter, which is large enough to allow the penetration of PdCl_4^{2-} ions ($5.7 \times 5.7 \times 3.4 \text{ \AA}^3$). Furthermore, the high loading amount of Pd NPs ($4.4 \pm 0.1 \text{ wt. \%}$, determined by ICP-OES through three parallel specimens) in our study compared with other works reported in literatures, which usually does not exceed 3 wt. % by using the same wetness impregnation process could also lend a support that part of the Pd NPs are embedded within the frameworks of the support,^{32–34} as a lower loading amount will be obtained if particles are only surface-loaded. What's more, when Pd atoms penetrate into the inner pores of the host, they influence the structure factors of Bragg peaks, leading to the slight variation

of intensities of the diffraction peaks belonging to the ScBTC NMOFs in PXRD patterns. The decrease of overall textural values in N_2 sorption, likewise, can also be ascribed to the insertion of Pd NPs into the pores of NMOFs. In the meantime, although partial particles were located on the outer surface, most of them present a size less than 5 nm. Since larger sizes are usually obtained without stabilizing agents in the reduction process, we suppose that the pore windows can also provide somewhat confinement effect for the particle growth. These, then in turn illustrate the effective template synthesis of tiny Pd NPs either located inside or outside the pores by using the pore channels or aperture windows of MOFs as anchors to confine the growth of Pd NPs and further support them as well.

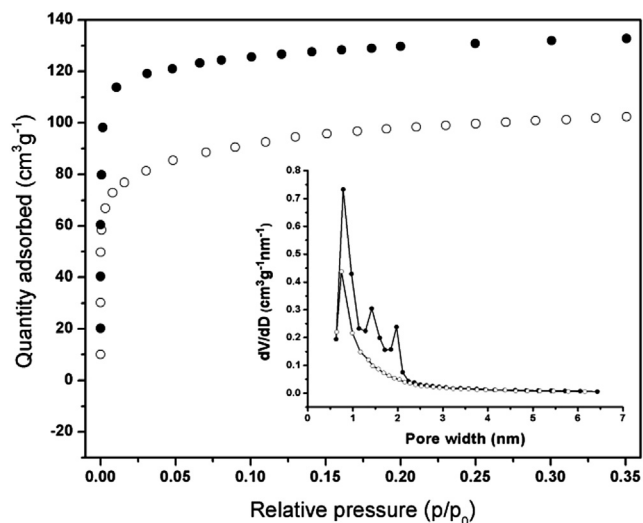


Fig. 4. Nitrogen sorption isotherms (77 K) for ScBTC NMOFs (black dots) and Pd-ScBTC NMOFs (white dots). Corresponding pore diameter distribution curves are shown in the inset.

To elucidate the nature of Pd supported particles, X-ray photoelectron spectroscopy (XPS) studies were undertaken for the catalyst (Fig. 5). The escape depth of the emitted electrons under the irradiation energies used is 20–30 Å, so XPS probes a depth of one or at most two MOF unit cells, which is sufficient to identify the oxidation state of the surface-loaded Pd NPs. Two well-defined peaks with binding energies of 335.55 and 340.8 eV are observed, which can be assigned to the signals of $3d_{5/2}$ and $3d_{3/2}$ levels of Pd^0 components, respectively. The binding energy difference of the two peaks is 5.25 eV, which is in accordance with the theoretical value. Therefore, the XPS analysis indicates that the in situ formed Pd NPs were thoroughly reduced to be neutral.

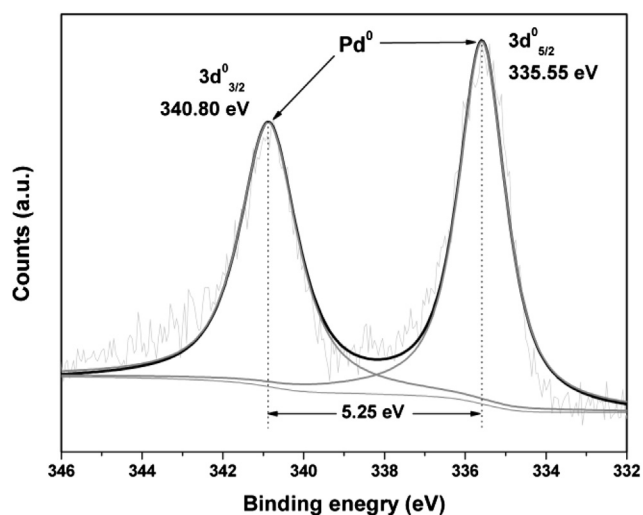


Fig. 5. X-ray photoelectron spectrum of Pd-ScBTC NMOFs.

Fourier transform infrared (FTIR) spectra analysis was performed to further clarify the oxidation state of those Pd NPs embedded within the frameworks (Fig. 6). The spectra of ScBTC NMOFs and Pd-NMOFs show no significant differences, as expected. In contrast with the standard IR spectrum of trimesic acid, the three main characteristic peaks attributed to the vibration of

$\nu(\text{O-H})$, $\nu(\text{C=O})$ and $\delta(\text{O-H})$ disappear. By contrast, both spectrums present newly observed absorption peaks. The bands $\nu_{\text{asym}}(\text{COO}^-)$ and $\nu_{\text{sym}}(\text{COO}^-)$ are found at 1607, 1554 cm^{-1} and 1447, 1391 cm^{-1} , respectively, which partly overlap with the vibration frequencies of the benzene ring skeleton causing the originally weak vibration peak at 1554 cm^{-1} becomes stronger. This confirms the bridging mode of the carboxylate group in the compound. The vibration frequency of Pd–O bond was reported in the region of 400–650 cm^{-1} ,³⁵ however, no absorption peaks within this region are observed for Pd-ScBTC NMOFs (see the insetted figure in Fig. 6), implying that ScBTC NMOFs act as solid solvent to support and disperse Pd NPs via electrostatic interaction rather than the direct Pd–O covalent bonding. The electrostatic interaction originates from the electron-donation from the electron-rich carbonyl portal of the organic moiety of NMOFs to the surface atoms of Pd NPs, which is weaker than covalent interaction, and thus Pd NPs may retain high chemical activities.³⁶

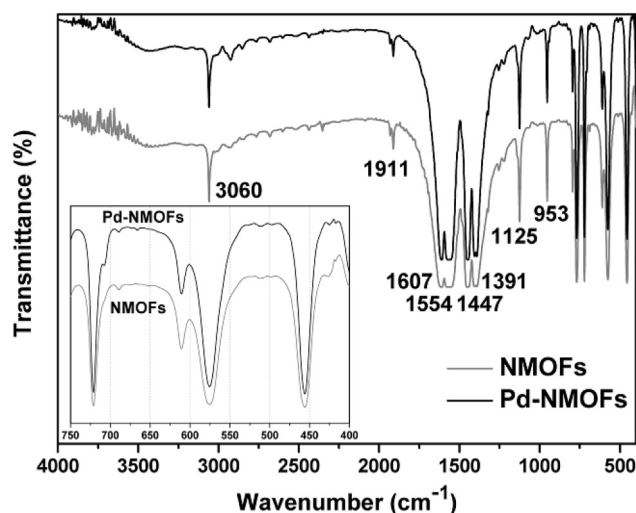


Fig. 6. FTIR spectra of ScBTC NMOFs and Pd-ScBTC NMOFs. The inset is the magnification of the spectrum in the range from 400 cm^{-1} to 750 cm^{-1} .

The thermogravimetric analysis (TGA) curves (Fig. 7) reveal the superior thermal stability of both the NMOFs and the Pd-NMOFs up to 500 °C. There is a 4% difference of $(\Delta w_2 - \Delta w_1)$ between NMOFs and Pd-NMOFs due to the Pd loading. In addition, PXRD patterns of

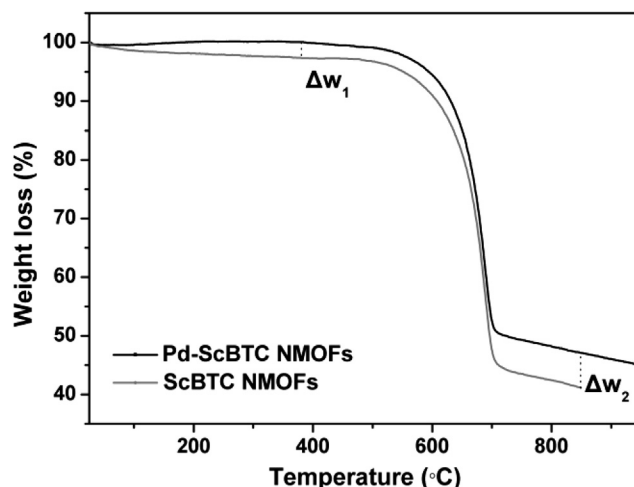


Fig. 7. TGA curves of ScBTC NMOFs and Pd-NMOFs under nitrogen atmosphere.

the support at various temperatures were obtained by heating the NMOFs in air to the given temperature and kept for 5 h (Fig. S3). The results indicate that the frameworks could retain unbroken up to 400 °C, and the organic components began to decompose with the temperature increasing continuously.

2.2. Evaluation of catalytic reactivity in Suzuki–Miyaura cross-coupling reaction

Suzuki–Miyaura coupling reaction with a set of substrates of aryl/heteroaryl halides and arylboronic acids were chosen to evaluate the activity of the catalyst and the results are presented in Table 1. High yields were easily obtained in a short time at room temperature when aryl iodides were used (>99% for GC yield, entries 1–2 in Table 1). It is well known that electronic effects strongly affect the Suzuki cross-coupling reactions. Compared with electron-rich *para*-substituted aryl halides, electron-deficient *para*-substituted aryl halides show higher activity in the process of coupling with arylboronic acids due to the activation of the benzene ring as well as the ease of the charge-transfer, while it is the

opposite in the case of *para*-substituted arylboronic acids. However, high catalytic activities were observed for both electron-rich *para*-substituted aryl bromides and electron-deficient *para*-substituted arylboronic acids under a relatively mild condition (40 °C for 0.5 h in air), and excellent yields of different cross-coupling products were approached (>91% for GC yield, entries 3–8 in Table 1). Noteworthy is that 2-bromoanisole, which contains electron-donating group and is sterically hindered, also gave an excellent yield (entry 9, Table 1). However, when the less active aryl chloride was employed, a poor GC yield of 22% was observed (80 °C for 1 h in air, entry 10 in Table 1). Extending the reaction time from 1 h to 10 h, the yield only increased slightly from 22% to 35% (entry 11, Table 1). A moderate yield of 46% was obtained by further doubling both the amount of catalyst used and the reaction time under N₂ atmosphere (entry 12, Table 1). Interestingly, when we replaced K₂CO₃ by NaOCH₃ as the base, the yield remarkably improved to 63% (entry 13, Table 1). Moreover, to our delight, the addition of tetrabutylammonium bromide (TBAB) enhanced the yield of the desired biaryl products from 63% to 75% (entry 14, Table 1), presumably owing to the stabilization effect of the Pd NPs.^{37,38} The

Table 1

Representative Suzuki–Miyaura cross-coupling reaction performed using the Pd–ScBTC NMOFs catalyst^a

$$\text{R}^1\text{-Ar-X} + \text{R}^2\text{-Ar}'\text{-B(OH)}_2 \xrightarrow[\text{H}_2\text{O / EtOH (1:1)}]{\text{Pd-ScBTC NMOFs}} \text{R}^1\text{-Ar-Ar}'\text{-R}^2$$

X = I, Br, Cl R = CH₃, OH, OCH₃, CN, NO₂, COOH Ar' = Ph

Entry	Halide substrate	X	R ¹	R ²	Base	Additive	T/°C	Time/h	Yield ^b /%
1		I	H	H	K ₂ CO ₃	—	40	0.5	97 (99)
2		I	4-OCH ₃	4-OCH ₃	K ₂ CO ₃	—	40	0.5	95 (99)
3		Br	H	H	K ₂ CO ₃	—	40	0.5	94 (99)
4		Br	4-CH ₃	H	K ₂ CO ₃	—	40	0.5	92 (98)
5		Br	4-OH	H	K ₂ CO ₃	—	40	0.5	93 (96)
6		Br	H	4-CN	K ₂ CO ₃	—	40	0.5	91 (93)
7		Br	H	4-NO ₂	K ₂ CO ₃	—	40	0.5	89 (91)
8		Br	4-OCH ₃	4-OCH ₃	K ₂ CO ₃	—	40	0.5	88 (93)
9		Br	2-OCH ₃	H	K ₂ CO ₃	—	40	0.5	87 (90)
10		Cl	H	H	K ₂ CO ₃	—	80	1.0	18 (22)
11		Cl	H	H	K ₂ CO ₃	—	80	10	31 (35)
12 ^c		Cl	H	H	K ₂ CO ₃	—	80	20	43 (46)
13 ^c		Cl	H	H	NaOMe	—	80	20	58 (63)
14 ^d		Cl	H	H	NaOMe	TBAB	80	20	75 (78)
15 ^d		Cl	4-COOH	H	NaOMe	TBAB	80	20	79 (83)
16 ^d		Cl	4-NO ₂	H	NaOMe	TBAB	80	20	82 (86)
17 ^d		Cl	4-OCH ₃	4-OCH ₃	NaOMe	TBAB	80	20	71 (75)
18 ^e		Cl	H	H	NaOMe	TBAB	80	20	93 (95)
19 ^f		Br	H	H	K ₂ CO ₃	—	40	0.5	Trace
20 ^e		Cl	H	H	NaOMe	TBAB	80	20	86 (90)
21		Br	H	H	K ₂ CO ₃	—	40	0.5	88 (92)
22		Br	H	H	K ₂ CO ₃	—	40	0.5	95 (99)
23		Br	H	4-OCH ₃	K ₂ CO ₃	—	40	0.5	97 (99)
24		Br	H	4-CN	K ₂ CO ₃	—	40	0.5	91 (95)

^a Reaction conditions: aryl/heteroaryl halide (1 mmol, 1 equiv), arylboronic acid (1.2 mmol, 1.2 equiv), K₂CO₃ (3 mmol, 3 equiv), Pd–ScBTC NMOFs (0.012 g, 0.5 mol % Pd), solvent: H₂O–EtOH (volume ratio: 1:1, 4 mL), stirring speed: 400 rpm. At the completion of the reaction, the solution was extracted with ethyl acetate and analyzed by GC and GC–MS.

^b Isolated yields (Yields determined by GC with *n*-dodecane as the external standard. Response factors were determined by calibration of standards).

^c Pd–ScBTC NMOFs (0.024 g, 1.0 mol % Pd), under N₂.

^d Pd–ScBTC NMOFs (0.024 g, 1.0 mol % Pd), 0.5 mmol TBAB, under N₂.

^e Halide substrate (0.5 mmol), arylboronic acid (0.6 mmol), 1.5 mmol NaOMe, Pd–ScBTC NMOFs (0.024 g, 2.0 mol % Pd), 0.25 mmol TBAB, under N₂.

^f Catalyst was filtrated off when the conversion of the reaction was 50% and the hot filtrate was further used as catalyst for a control experiment.

introduction of electron-deficient *para*-substituted functional groups can further facilitate the activation of aryl chlorides, thus the yields slightly improved by 5–8% under the same conditions (entries 15–17, Table 1). It is worth mentioning that when halving the amount of the substrates, the yield can reach as high as 95% (entry 18, Table 1). We then further extended the scope of reaction substrates to pyridyl halides, and generally good yields can also be obtained. 3-Chloride-pyridine was coupled with phenylboronic acid to afford the target product in 90% yield in 20 h (entry 20, Table 1), which was comparable with the result of using the corresponding aryl chloride as the substrate under the same reaction conditions. The position of the halide on the heteroaromatic ring influenced the efficiency of the reaction, and a lower yield was obtained for 2-bromide-pyridine compared with 3-bromide-pyridine (92% and 99%, respectively, entries 21 and 22, Table 1). Again, the electronic property of the substituent group has a poor influence on the reactivity of pyridyl bromides, and 95–99% yields were obtained (entries 22–24, Table 1). These experiments can be repeated easily with the similar high yields, indicating the excellent performance of the catalyst.

Surface science studies show that aryl chlorides adsorb on Pd (111) surfaces mainly via π -electrons, resulting in a nearly parallel orientation of the ring with the surface.³⁹ Adsorption of the aryl moiety to the Pd surface serves as an anchor, enhancing the chemical interaction of the C–Cl bond with a separate but nearby Pd site (i.e., an anchimeric effect). Furthermore, the adsorption of aryl chlorides influences the electronic properties of the catalytic surface in the presence of TBAB.⁴⁰ It leads to a decrease in the work function of the metal surface, implying a net electron flow from the adsorbed aryl group to the Pd surface.⁴¹ The Pd surface acts effectively as an electron-withdrawing substituent on the aryl ring, which facilitates C–Cl bond activation. The corresponding increase in electron density on Pd, in turn, facilitates C–Cl bond activation. These cooperative anchimeric and electronic effects are absent with single-site homogeneous Pd catalyst, which may explain the excellent reactivity of Pd-ScBTC NMOFs catalyst for aryl chlorides activation.

For comparison, commercial 5 wt. % Pd/C catalyst (0.021 g, 1.0 mol % Pd) and bulk ScBTC MOFs-supported Pd catalyst (Pd-ScBTC MOFs, 3.2 wt. %, 0.033 g, 1.0 mol % Pd) were also studied by employing aryl chloride and phenylboronic acid as the substrate in the solvents of H₂O, EtOH–H₂O (1:1) and DMF–H₂O (1:1) respectively, while keeping the other reaction conditions the same as entry 14 of Table 1. The results (Fig. 8) show a same trend in conversion (Pd/C < Pd-MOFs < Pd-NMOFs) but a slight difference in activity differing from the solvent used in the sequence of H₂O < EtOH–H₂O < DMF–H₂O. The commercial Pd/C generally presented unsatisfactory results with yield range from 18% to 36%. By contrast, the as-synthesized Pd-ScBTC NMOFs catalyst attained 48% yield in the presence of pure water, and further afforded 78% and 82% higher yield in the EtOH–H₂O and DMF–H₂O system, respectively. While the corresponding bulk ScBTC MOFs supported Pd catalyst showed inferior performance, with products obtained in the yield range of 37–75% under the same conditions. This suggests that our composite is an efficient catalyst, which may be applied to other challenging substrates. We have carried out an analogous TEM study of commercial Pd/C (Fig. S4). TEM analyses show that the particle size distribution of Pd NPs in active carbon was significantly broader with a considerable number of Pd particles larger than that in Pd-NMOFs. In the reduction process of activated carbons, the presence of a variety of different functional groups that interact differently with metal ions would lead to a less homogeneous initial distribution of Pd²⁺ with formation of larger agglomerates than the template-synthesized Pd NPs in ScBTC NMOFs, although an in-depth understanding of the reduction process on ScBTC NMOFs is still needed. It is well known that the activity of

palladium-supported catalyst depends dramatically on the metal dispersion and the particle size. Probably for this reason, the activity of palladium NPs supported on ScBTC NMOFs is higher than that of Pd supported on activated carbon. While in the case of Pd-ScBTC MOFs, observed as solid bulks (Fig. S5), the inferior performance is mainly due to the lower surface area of 366 m² g⁻¹ (Fig. S6). The large surface area created by the support can effectively facilitate both the Pd leaching into the solution to catalyze the reaction and the re-deposition of the leached Pd on the surface of the support after the reaction is completed.

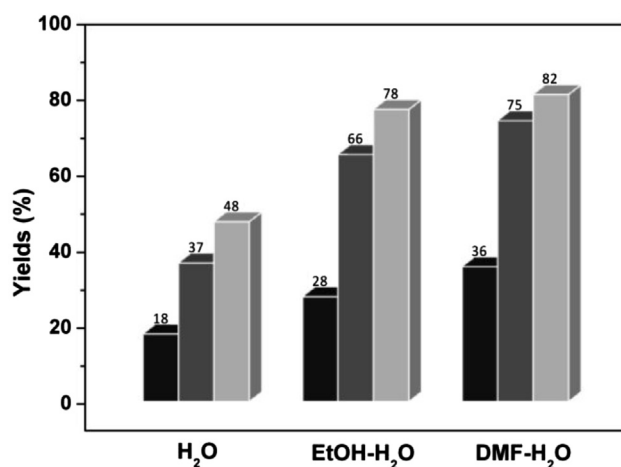


Fig. 8. Catalytic activity comparison of Pd-ScBTC NMOFs (light gray columns), ScBTC MOFs (gray columns) and Pd/C (black columns) in the solvent of H₂O, EtOH–H₂O (1:1) and DMF–H₂O (1:1).

We tested the leaching of Pd NPs by coupling bromobenzene with phenylboronic acid in the presence of the Pd-ScBTC NMOFs catalyst in EtOH–H₂O (1:1) mixture (entry 19, Table 1). When the conversion of the reaction was 50% (10 min, GC), the catalyst was filtered off and the hot filtrate was allowed to react further. The formation of the ‘cross-coupled’ biphenyl or any other conversion products were also observed in 1% yield, thus indicating that aromatic nucleophilic substitution took place to a small extent, which caused by some active species, either dissolved or as heterogeneous particles. These, however, lose activity quickly. Furthermore, after catalyst filtration we observed less than 1.0 ppm Pd (i.e., <0.20% loss based on the initial palladium, determined by ICP-OES) in the reaction mixtures, which lends support that the reaction was heterogeneously catalyzed.

To evaluate the recyclability of the Pd-NMOFs catalyst system, the couplings with iodobenzene and phenylboronic acid as substrates were carried out under the same condition as entry 1 of Table 1 for five times, and the results are shown in Table 2. The catalyst could be recovered easily without either detectable loss of activity or extension of the reaction time in the first three catalytic

Table 2
Investigation into the reuse of Pd-ScBTC NMOFs catalyst^a

Number of catalytic cycles	1	2	3	4	5
Yield ^b /%	>99	>99	>99	97	94

^a Reaction conditions: iodobenzene (1 mmol, 1 equiv), phenylboronic acid (1.2 mmol, 1.2 equiv), K₂CO₃ (3 mmol, 3 equiv), Pd-ScBTC NMOFs (0.012 g, 0.5 mol % Pd), solvent: H₂O–EtOH (volume ratio: 1:1, 4 mL), stirring speed: 400 rpm. After each run, the catalyst was isolated by centrifuge. Washed with ethanol, and dried for the next cycle.

^b Yields determined by GC using an external standard method based on aryl halide.

cycles and the activity only decreased slightly from the fourth cycle, and the framework of the recovered catalyst was completely unchanged after five runs (Fig. 1c), proving that the catalyst possessed high chemical activity and good stability. Additionally, the same yield could be obtained after the catalyst was kept in air for several weeks, further confirming the high activity and stability of the catalyst.

3. Conclusions

In summary, catalytic Pd nanoparticles have been successfully synthesized and further supported by using nanoscale scandium-organic framework as a novel template and support through a microwave-assisted method. It is found that ScBTC NMOFs act as solid solvent to support and disperse Pd NPs via electrostatic interaction rather than Pd–O covalent bonding. Thus the synthesized Pd–ScBTC NMOFs exhibits high catalytic activity and good stability in the Suzuki cross-coupling reaction, and superior performances are observed compared to either the bulk MOFs or active carbon supported Pd catalyst. Notably, the catalyst shows negligible metal leaching and can be recovered without significant activity loss after several catalytic cycles. In view of the highly porosity, size miniaturization and the resulting high surface area, nanoscale MOFs as support materials for the loading of catalytic particles ensures competitive advantage over bulk materials for enhanced catalytic activity. A key issue for our future studies will be to identify NMOFs with higher chemical stability and robustness allowing for a broader range of catalytic reactions.

4. Experimental section

4.1. Synthesis and characterization

Starting materials and solvents were purchased from commercial resources and used as received. The synthesis of materials was assisted by a microwave apparatus (Biotage, Initiator™ Eight). The chemical composition of the impregnated material was determined by an inductively coupled plasma optical emission spectrometer (ICP-OES, Jobin Yvon Ultima2). Structural characterization of ScBTC NMOFs and Pd–ScBTC NMOFs were recorded by powder X-ray diffraction (PXRD) using a Rigaku X-ray diffractometer (Miniflex II, Cu K α , 30 kV, 15 mA). Microstructural analyses were performed by scanning electron microscopy (JEOL JSM-6700F SEM) and transmission electron microscopy (JEOL JEM-2010 TEM, operating at 200 kV with a point resolution of 0.23 nm). The texture properties were determined from nitrogen adsorption/desorption isotherms at 77 K measured with a Micromeritics ASAP 2020 apparatus. The specific surface area was obtained by multiple-point Brunauer–Emmett–Teller (BET) method, the total pore volume was computed from the amount of gas adsorbed at $p/p_0=0.99$, and the pore diameter distribution was determined by Horvath–Kawazoe (HK) model applied to the adsorption branch of the isotherms. Thermogravimetric analysis (TGA) was performed from 30 °C to 1000 °C in a nitrogen atmosphere with a Netzsch STA449C instrument at a heating rate of 10 K/min. X-ray photoelectron spectroscopy (XPS) measurements were carried on a Thermo Scientific ESCALAB 250. Binding energies were calibrated by using the containment carbon (C1s=284.6 eV). Fourier transform infrared (FTIR) spectra was obtained by using a PerkinElmer Spectrum One instrument with sample prepared as KBr pellets at wavenumbers range from 400 to 4000 cm^{-1} . Gas chromatography (GC) and gas chromatography–mass spectrometer (GC–MS) analysis of the reaction mixture and the isolated products were performed on a Varian 430-GC system by using an external standard method and Varian 450-GC/240-MS, respectively. ^1H and ^{13}C NMR spectra were recorded on a BRUKER BIOSPIN AVANCE III (400 MHz) spectrometer

using CDCl_3 or $\text{DMSO}-d_6$ as solvent and chemical shift values were expressed in parts per million (ppm) from tetramethylsilane (TMS) as an internal standard.

ScBTC NMOFs were synthesized by a surfactant-assisted microwave irradiation method from a mixture of trimesic acid (53 mg, 0.25 mmol), scandium nitrate aqueous solution (0.4 M, 625 μL), triethylamine (100 μL) and cetrimonium bromide (CTAB, 0.03 mmol) in ca. 5 mL distilled water. This solution was heated by microwave in sealed vessels at 300 W for 15 min at 150 °C. The resulting particles were isolated by centrifugation (4500 rpm, 5 min), washed with ethanol and water for several times by sonication followed by centrifugation and then dried under vacuum at 45 °C for 12 h. Yield: 75.4% (based on Sc).

ScBTC MOFs were synthesized under hydrothermal condition within a Teflon-lined Parr autoclave from a mixture of trimesic acid (53 mg, 0.25 mmol), scandium nitrate aqueous solution (0.4 M, 625 μL) and triethylamine (100 μL) in ca. 5 mL distilled water. After the reaction mixture was stirred to homogeneity, the autoclave was sealed and heated for 2 days at 150 °C under autogenous pressure. After reaction, the precipitate was isolated by centrifugation (4500 rpm, 5 min), washed with distilled water (3 \times 10 mL) and ethanol (3 \times 5 mL) alternately, and then dried under vacuum at 45 °C for 12 h. The resulting product was obtained as white powder in 87.9% yield (based on Sc).

ScBTC NMOFs supported Pd catalyst was prepared as follows: 0.1 g of the activated ScBTC NMOFs (150 °C under dynamic vacuum for 12 h) and an appropriate amount of chloropalladic acid (H_2PdCl_4) solution containing ca. 5 wt. % Pd were sonicated in a sonication bath until a homogeneous yellowish-white suspension was obtained, and then stirred for another 12 h at room temperature. The solution was placed inside a conventional microwave after adding 100 μL of the reducing agent hydrazine hydrate (HH). The microwave oven was then operated at full power (300 W, 2.45 GHz) for 5 min. After reaction, the yellow solution of PdCl_4^{2-} -NMOFs changed to a black color, and the precipitate was centrifugally isolated and washed with water and ethanol alternatively, then dried under vacuum. Pd–ScBTC NMOFs were obtained as gray powder in 75.0% yield (based on Pd).

ScBTC MOFs supported Pd catalyst was prepared as the same procedure as the Pd–ScBTC NMOFs mentioned above.

4.2. Catalytic reaction

4.2.1. General procedure for the Pd–ScBTC NMOFs catalyzed Suzuki coupling reaction. Typically, all solid reagents were weighted into an oven-dried 25 mL Schlenk flask, which was equipped with a magnetic stir bar, septum, and a condenser. The liquid compounds were then introduced by syringe, with the aryl/heteroaryl halide always as the last addition. The flask was immersed in an oil bath and stirred at desired temperature, while the extent of the reaction was monitored by TLC analysis. When the reaction was complete, the solid was removed by centrifugation and washed with ethanol and water alternately and recovered for further consecutive runs. The filtrate was collected and extracted with diethyl ether (3 \times 10 mL), and the ether layer was washed with a saturated brine solution. The extract was dried with anhydrous sodium sulfate, and then concentrated under reduced pressure. The residue was purified by flash chromatography on silica gel using a certain proportional mixture of petroleum ether and ethyl acetate as an eluent, and followed by a recrystallization process to provide the desired biaryl derivatives. The structures of all the products were unambiguously established on the basis of their spectral analysis (^1H NMR and ^{13}C NMR spectral data, see the [Supplementary data](#)).

4.2.2. The reuse of the catalyst. After the first run of the coupling reaction between iodobenzene and phenylboronic acid, the catalyst

was isolated by centrifuge, and washed with ultrapure water (2×10 mL) and ethanol (2×10 mL). The recovered catalyst was transferred to a 25 mL Schlenk flask, then base (3 mmol), phenylboronic acid (1.2 mmol) and iodobenzene (1 mmol) were added in sequence, and the mixture was heated under stirring for a certain time. The product was isolated following the procedure as the first run and the catalyst was collected and used for the next cycle.

Acknowledgements

This work was supported by grants of 973 programs (2013CB933203), the National Nature Science Foundation of China (21071143, 21131006) and Nature Science Foundation of Fujian Province.

Supplementary data

Supplementary data related to this article can be found at <http://dx.doi.org/10.1016/j.tet.2013.08.059>.

References and notes

- Hodes, G. *Adv. Mater.* **2007**, *19*, 639.
- Balanta, A.; Godard, C.; Claver, C. *Chem. Soc. Rev.* **2011**, *40*, 4973.
- Gonzalez, S. B.; Rodriguez, M. J.; Blanco, C.; Rivas, J.; Lopez-Quintela, M. A.; Martinho, J. M. G. *Nano Lett.* **2010**, *10*, 4217.
- Huang, X.; Tang, S.; Liu, B.; Ren, B.; Zheng, N. *Adv. Mater.* **2011**, *23*, 3420.
- Wang, X.; Zhuang, J.; Peng, Q.; Li, Y. *Nature* **2005**, *437*, 121.
- Zhou, Z. Y.; Tian, N.; Li, J. T.; Broadwell, I.; Sun, S. G. *Chem. Soc. Rev.* **2011**, *40*, 4167.
- Zhuang, Z.; Peng, Q.; Li, Y. *Chem. Soc. Rev.* **2011**, *40*, 5492.
- Yang, C. M.; Sheu, H. S.; Chao, K. J. *Adv. Funct. Mater.* **2002**, *12*, 143.
- Escola, J. M.; Aguado, J.; Serrano, D. P.; Garcia, A.; Peral, A.; Briones, L.; Calvo, R.; Fernandez, E. *Appl. Catal., B* **2011**, *106*, 405.
- Cano, M.; Benito, A.; Maser, W. K.; Urriolabeitia, E. P. *Carbon* **2011**, *49*, 652.
- Han, J.; Liu, Y.; Guo, R. J. *Am. Chem. Soc.* **2009**, *131*, 2060.
- Sarkar, J.; John, V. T.; He, J.; Brooks, C.; Gandhi, D.; Nunes, A.; Ramanath, G.; Bose, A. *Chem. Mater.* **2008**, *20*, 5301.
- Hermes, S.; Schröter, M. K.; Schmid, R.; Khodeir, L.; Muhler, M.; Tissler, A.; Fischer, R. W.; Fischer, R. A. *Angew. Chem., Int. Ed.* **2005**, *44*, 6237.
- Jacobs, B. W.; Houk, R. J. T.; Anstey, M. R.; House, S. D.; Robertson, I. M.; Talin, A. A.; Allendorf, M. D. *Chem. Sci.* **2011**, *2*, 411.
- Vilhelmsen, L. B.; Walton, K. S.; Sholl, D. S. *J. Am. Chem. Soc.* **2012**, *134*, 12807.
- Houk, R. J. T.; Jacobs, B. W.; Gabaly, F. E.; Chang, N. N.; Talin, A. A.; Graham, D. D.; House, S. D.; Robertson, I. M.; Allendorf, M. D. *Nano Lett.* **2009**, *9*, 3413.
- Park, Y. K.; Choi, S. B.; Nam, H. J.; Jung, D. Y.; Ahn, H. C.; Choi, K.; Furukawa, H.; Kim, J. *Chem. Commun.* **2010**, 3086.
- Jiang, H. L.; Lin, Q. P.; Akita, T.; Liu, B.; Ohashi, H.; Oji, H.; Honma, T.; Takei, T.; Haruta, M.; Xu, Q. *Chem.—Eur. J.* **2011**, *17*, 78.
- Jiang, H. L.; Akita, T.; Ishida, T.; Haruta, M.; Xu, Q. *J. Am. Chem. Soc.* **2011**, *133*, 1304.
- Jiang, H. L.; Liu, B.; Akita, T.; Haruta, M.; Sakurai, H.; Xu, Q. *J. Am. Chem. Soc.* **2009**, *131*, 11302.
- Li, P. Z.; Aranishi, K.; Xu, Q. *Chem. Commun.* **2012**, 3173.
- Gao, S.; Zhao, N.; Shu, M.; Che, S. *Appl. Catal., A* **2010**, *388*, 196.
- Yuan, B.; Pan, Y.; Li, Y.; Yin, B.; Jiang, H. *Angew. Chem., Int. Ed.* **2010**, *49*, 4054.
- El-Shall, M. S.; Abdelsayed, V.; Khder, A. E. R. S.; Hassan, H. M. A.; El-Kaderi, H. M.; Reich, T. E. *J. Mater. Chem.* **2009**, *19*, 7625.
- Carne, A.; Carbonell, C.; Imaz, I.; Maspocho, D. *Chem. Soc. Rev.* **2011**, *40*, 291.
- Zhang, J.; Sun, L.; Xu, F.; Li, F.; Zhou, H. Y.; Liu, Y. L.; Gabelica, Z.; Schick, C. *Chem. Commun.* **2012**, 759.
- Qiu, L. G.; Li, Z. Q.; Wu, Y.; Wang, W.; Xu, T.; Jiang, X. *Chem. Commun.* **2008**, 3642.
- Jiang, D.; Burrows, A. D.; Edler, K. J. *CrystEngComm* **2011**, *13*, 6916.
- Della Rocca, J.; Lin, W. B. *Eur. J. Inorg. Chem.* **2010**, *24*, 3725.
- Taylor-Pashow, K. M. L.; Della Rocca, J.; Huxford, R. C.; Lin, W. B. *Chem. Commun.* **2010**, 5832.
- Rocca, J. D.; Liu, D.; Lin, W. B. *Acc. Chem. Res.* **2011**, *44*, 957.
- Sabo, M.; Henschel, A.; Frode, H.; Klemm, E.; Kaskel, S. J. *Mater. Chem.* **2007**, *17*, 3827.
- Cheon, Y. E.; Suh, M. P. *Angew. Chem., Int. Ed.* **2009**, *48*, 2899.
- Hwang, Y. K.; Hong, D. Y.; Chang, J. S.; Jhung, S. H.; Seo, Y. K.; Kim, J.; Vimont, A.; Daturi, M.; Serre, C.; Férey, G. *Angew. Chem., Int. Ed.* **2008**, *47*, 4144.
- Kramareva, N. V.; Stakheev, A. Y.; Tkachenko, O. P.; Klementiev, K. V.; Grunert, W.; Finashina, E. D.; Kustov, L. M. *J. Mol. Catal. A: Chem.* **2004**, *209*, 97.
- Jana, N. R.; Peng, X. *J. Am. Chem. Soc.* **2003**, *125*, 14280.
- Bedford, R. B.; Blake, M. E.; Butts, C. P.; Holder, D. *Chem. Commun.* **2003**, 466.
- Reetz, M. T.; de Vries, J. G. *Chem. Commun.* **2004**, 1559.
- Richardson, N. V.; Palmer, N. R. *Surf. Sci. Lett.* **1982**, *114*, L1.
- Aarts, J. F. M.; Phelan, K. G. *Surf. Sci.* **1989**, *222*, L853.
- Diefenbach, A.; Bickelhaupt, F. M. *J. Phys. Chem. A* **2004**, *108*, 8460.